30th AIAA Applied Aerodynamics Conference
25-28 June 2012, New Orleans, Louisiana
2012-3026

Low-to-Moderate Aspect Ratio Wings Tested at Low Reynolds Numbers

Gavin K. Ananda,* Pritam P. Sukumar† and Michael S. Selig‡
University of Illinois at Urbana-Champaign, Urbana, IL 61801

This paper presents wind tunnel results of wings of low-to-moderate aspect ratio ($2 \leq AR \leq 5$) at low Reynolds numbers (60,000 to 160,000). Tests were conducted in the low-turbulence wind tunnel in the Subsonic Aerodynamics Research Laboratory at the University of Illinois at Urbana-Champaign (UIUC). A 3-component force/moment balance was designed and fabricated. The balance design methodology and validation are described in detail. Low Reynolds number tests performed on a wing having an aspect ratio of 4 and using the Wortmann FX 63-137 airfoil showed the existence of a critical Reynolds number of 90,000 for which a jump in performance characteristics was observed. Pre-stall and post-stall hysteresis was captured at the critical Reynolds number. Flow visualization photographs for the wing at different angles of attacks are presented. Finally, aerodynamic performance measurements taken for ten flat-plate rectangular and tapered wings are also presented and discussed.

I. Introduction

With the emergence of unmanned aerial vehicle (UAV) platforms as an integral part of the military, there has been a push to minimize the size of these vehicles to serve platoon-level roles and other forms of civilian aerial surveillance and reconnaissance missions. The initial drive for small-scaled UAVs came in the form of the MAV development initiative[1] from 1996–2002 by the Defense Advanced Research Project Agency (DARPA) and the Naval Research Laboratory (NRL). This initiative yielded a multitude of research in 6–12 in wingspan fixed wing MAVs as detailed in Refs. 1–20. Despite the large strides achieved in MAV research, the payload capacities and endurance levels of MAVs have not reached levels that are practical for use.[21] The current level of technology though has produced a plethora of small UAVs (i.e., man-portable and hand-launch UAVs) that are in service both in military and civilian environments. Most UAVs (e.g., Desert Hawk, Wasp III, Raven) in this category are of low-to-moderate aspect ratios ($2 \leq AR \leq 7$) and operate at Reynolds numbers between 50,000 and 300,000.

It is commonly noted[18,22] that with a few exceptions[12,13,20,23–25] there is a lack of experimental data related to low-to-moderate aspect ratio UAV flight at low Reynolds numbers. As a result, two-dimensional experimental data[26–30] is primarily used in the small UAV design process. However, the mutual interaction between the three-dimensional finite wing and low Reynolds number effects plays a large role. Hence, it is essential to have a comprehensive understanding of low Reynolds number wing characteristics in order to push the envelope of small UAV capabilities.

The goal of this paper is to show the beginnings of a concerted effort by the Applied Aerodynamics Group at the University of Illinois at Urbana-Champaign (UIUC) to address the issues discussed heretofore. Aerodynamic performance measurements for low-to-moderate aspect ratio wings taken using a custom designed and fabricated low-speed wind tunnel balance is presented. Flow visualization of the wing mounting setup and historical lift, drag and moment comparisons for two separate wings are presented to validate the

*Graduate Research Assistant, Department of Aerospace Engineering, AIAA Student Member.
†Graduate Research Assistant, Department of Aerospace Engineering, AIAA Student Member.
‡Associate Professor, Department of Aerospace Engineering, AIAA Member.

balance. Aerodynamic measurements for a Wortmann FX 63-137 aspect ratio ($\mathcal{AR}$) 4 rectangular wing are presented and discussed. To further aid in understanding the phenomena related to the wing, flow visualization was employed. Finally, ten rectangular and tapered flat-plate wings of aspect ratios between 2 and 5 were tested at Reynolds number between 60,000 and 160,000 using the low Reynolds number force balance (LRN-FB). Aerodynamic measurements of the ten wings are presented and discussed.

II. Experimental Methods

A. Facility

Experiments were conducted in the low turbulence subsonic wind tunnel in the Aerodynamics Research Laboratory at UIUC. Shown in Fig. 1, the wind tunnel is an open-return tunnel with a rectangular test section measuring 2.8×4.0 ft in cross-section and has a length of 8 ft. Over the length of the test section, the width increases by approximately 0.5 in (1.27 cm) to account for boundary layer growth along the tunnel side walls. Test section speeds up to 160 mph (71.53 m/s) can be obtained via a 125 hp (93.25 kW) alternating current electric motor connected to a five-bladed fan.

As detailed in Ref. 30, the turbulence intensity of the wind tunnel was measured to be less than 0.1%. This turbulence level allows for accurate measurement of low Reynolds number behavior as test section turbulence levels ensure that laminar flow does not prematurely transition to turbulent flow.

B. Force/Moment Balance

A custom designed and in-house fabricated three-component low Reynolds number force/moment balance (LRN-FB) was used to acquire all of the data presented in this paper. The experimental setup is depicted in Fig. 2. The LRN-FB was designed to be conceptually similar to the University of Notre Dame's UND-FB2 force/moment balance.[15] The LRN-FB resides on the ceiling of the test section, and the wings are mounted at quarter chord using a wing-tip mounted sting. The spanwise axis is in the vertical direction. The sting was designed to vary with the type of wing tested (i.e., thickness, camber, planform shape, etc.) and transfer the aerodynamic loads of the wing to the balance.

The balance consists of two perpendicularly mounted carriages that allowed it to measure principally lift and drag forces from the wing. Each carriage uses eight double-ended flexural pivot bearings (flex-pivots) manufactured by the Riverhawk Company. As discussed in Ref. 31, flexures are one of the main components of an external wind tunnel balance. They are designed to ensure that the balance reacts similarly in all principal directions and without hysteresis. Additional benefits of flex-pivots are that they are stiction-free

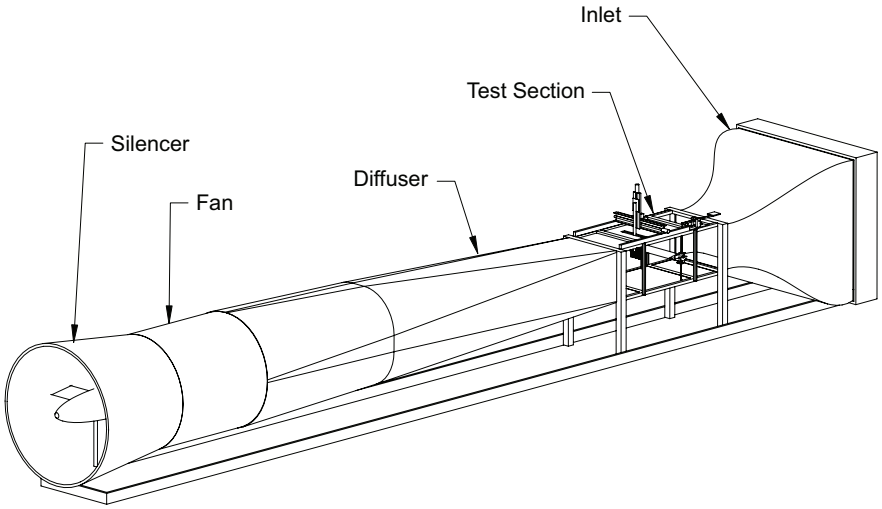

Figure 1. UIUC low-speed subsonic wind tunnel.

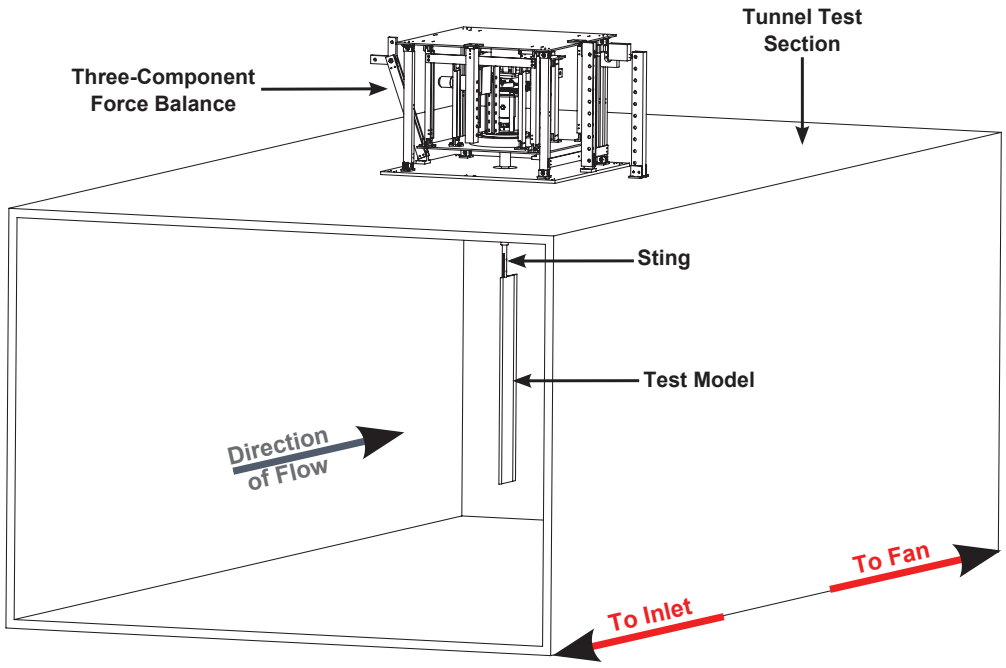

Figure 2. LRN-FB setup in tunnel test section.

and have, theoretically, infinite cycle life.

The lift carriage is the outer carriage on the base platform, and the drag carriage is suspended within the lift carriage. Both carriages are connected to load cells manufactured by Interface, Inc. via load cell mounting brackets. The mounting brackets can accept different load cell attachment points to allow for variations in the operational range of the lift and drag carriages. The carriages are pre-loaded to ensure that the load cells are always working in tension. This approach allows the force balance to be able to measure accurately both small and large forces occurring in the Reynolds number range of 60,000 to 160,000.

Within the drag carriage, a US Digital® A2 absolute optical encoder together with a DC gear motor to worm gear setup measures and sets the angle of attack of the wing respectively. The A2 optical encoder is an optical rotary position sensor that reports its shaft angle within a 360-deg range. The resolution of the optical encoder is 0.09 deg, and the zero position of its shaft can be reset to any location. The DC gear motor to worm gear setup is designed to be similar to the angle-of-attack setup of the UIUC Low Speed Airfoil Testing (LSATs) experimental rig.[27–30] A Faulhaber® 308:1 ratio DC gear motor runs a 48-pitch worm shaft via a rotational coupling. The worm shaft in turn rotates a 45:1 gear ratio, 180-teeth worm gear aligned in the axis of rotation of the spanwise axis of the wing. The drag carriage also houses a Transducer Techniques® RTS torque sensor that measures the aerodynamic pitching moment of the wing. Given that the torque sensor is unable to handle axial loads, an intricated setup was designed to house it. This setup includes a $\frac{5}{8}$-in diameter double-ended flexural pivot, two large tapered roller bearings and multiple fittings. The goals of the angle-of-attack and torque-sensor setups are two pronged:

- To allow the torque sensor to rotate with change in the angle of attack of the sting/wing. The non-measuring end of the torque sensor attaches directly to the worm gear allowing the torque sensor to measure the pitching moment of the wing at each angle of attack.
- To ensure that only the moment loads of the wing are transmitted to the torque sensor. A fitting attaches the measurement end of the torque sensor to the sting via the $\frac{5}{8}$-in flex-pivot. The central portion of the flexure is fixed with respect to the angle of attack thereby preventing the axial loads of the wing from reaching the torque sensor.

The components of the LRN-FB were fabricated and assembled to tolerance levels of ±0.002–0.005 in.

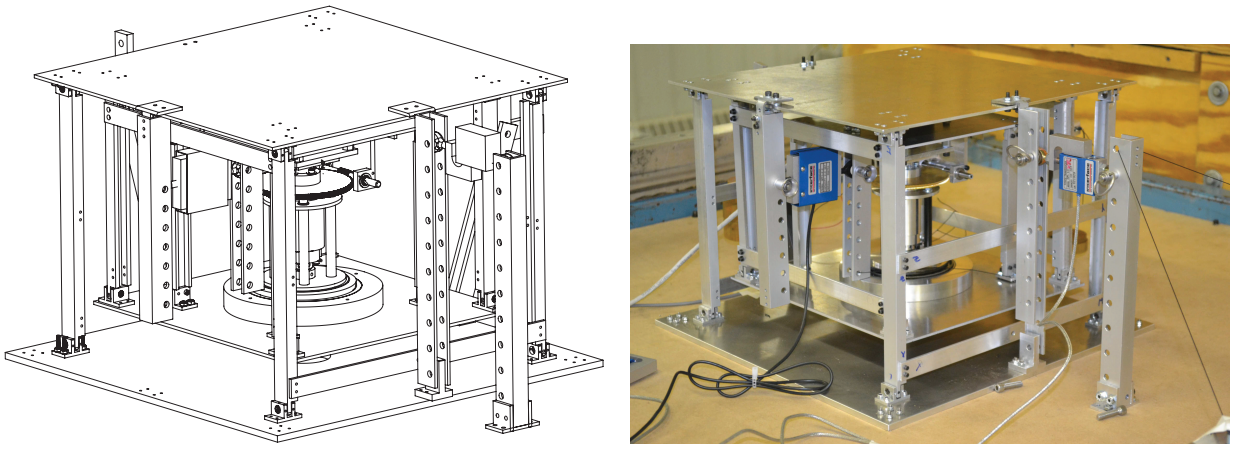

(a) (b)

Figure 3. UIUC LRN-FB three-component wind tunnel force balance: (a) CAD model and, (b) fabricated rig.

This tolerance level ensured that assembly of the balance was performed with minimal fitting issues. An isometric view of the CAD model and a photograph of the fabricated LRN-FB are shown in Fig. 3.

As built, the maximum, minimum and resolution forces that the LRN-FB was designed to measure are detailed in Table 1. The values that are asterisked are limits set solely by the maximum bending moment limit of the flex-pivot that attaches the sting to the torque sensor on the LRN-FB. If higher load measuring capabilities are required for future tests, a simple replacement of the $\frac{5}{8}$-in diameter flexure to one of a higher torsional spring rate would suffice as its bending moments limits increase with flexure diameter.

Although the LRN-FB was designed so that lift L, drag D, and moment M measured were pure and with minimal interactions, there always exists some first- or second-order interactions (e.g., lift and drag carriages not exactly perpendicular) between the different parts of the balance under loading. Therefore linear calibration was performed for lift and drag, and the moment was non-linearly calibrated by methods described in Refs. 32–34. To ensure that the effects of drift and other unrealized errors were taken into account, calibration was performed frequently. To account for interactions between the lift and drag carriages, a calibration matrix was derived according to the steps outlined in Ref. 31. Finally, during testing, wing drag polars were repeated at least two times in each case to ensure repeatability of data acquired.

C. Data Acquisition

A PC with a National Instruments NI PCI-6052E data acquisition board was used for communication with the wind tunnel and the force/moment balance. The National Instruments Labview® 2010 graphical user interface (GUI) software was used for recording and processing the raw force/moment and flow condition data during testing.

Test section dynamic pressure was measured with a differential pressure transducer in the wind tunnel inlet and test section. Ambient temperature was measured with a thermocouple. Lift, drag and moment data from the load cell were passed through a signal conditioner to amplify and filter the signal for the DAQ board. At each angle of attack, 30,000 samples of lift, drag and moment data measured at a rate of 3,000 samples/sec were averaged to overcome the small time-dependent fluctuations in tunnel speed.

Table 1. Force Balance Loads Measurements Characteristic

Property	Units	Maximum	Minimum	Resolution
L	lb (g)	2.50* (1134*)	−2.50* (−1134)	0.0013 (0.6)
D	lb (g)	2.50* (1134*)	0.01 (0.5)	0.0013 (0.6)
M_{ac}	ft-lb (in-oz)	0.46 (89.1)	−0.46 (−89.1)	0.0003 (0.06)

Table 2. Flat-Plate Model Test Matrix.

	Aspect Ratio			
	2	3	4	5
λ	0.5	0.5	0.5	-
	0.75	0.75	0.75	-
	1	1	1	1

Each run involved taking measurements of the wing for both increasing and decreasing angles of attack in succession to capture any possible aerodynamic hysteresis. The DC angle of attack motor was controlled via a custom-designed motor controller.

During a run, the entire data-acquisition process was automated. The Labview® interface set and maintained the Reynolds number within the test section and angle of attack of the wing, acquired raw data (dynamic pressure, lift, drag, pitching moment, angle of attack, ambient temperature and ambient pressure), and finally reduced and plotted the data graphically during a run. Once the run was complete, the data was corrected for three-dimensional tunnel effects according to the methods outlined in Ref. 31.

The relative uncertainties of the lift, drag and moment coefficents were calculated to be 3.3%, 2.7% and 4.6% respectively using the methods introduced by Kline and McClintock[35] and further discussed by Coleman and Steel.[36]

III. Models Tested

All of the models tested in this paper were rapid prototyped using stereolithography (SLA®) to tolerances of approximately ± 0.005 in,[37] ensuring model accuracy and surface quality.

As a test validation case, the Wortmann FX 63-137 $\mathcal{AR}$ 4 rectangular wing was chosen. The availability of experimental data in literature[23,38] made it a good choice for validation. An aspect ratio of 4 was chosen as it represented the mean aspect ratio of wings intended to be tested with the balance.

To aid in validation, an additional rectangular flat-plate $\mathcal{AR}$ 3 wing was chosen as a benchmark for low aspect ratio flat-plate measurements. The $\mathcal{AR}$ 3 flat-plate wing was designed to emulate that tested by Pelletier and Mueller,[13] and Shields and Mohseni.[20] The key differences though was that the thickness-to-chord ratio of the flat-plate model was 4.3% in comparison with 2.6% in Ref. 13. In addition, the flat-plate model was designed to have a 10-to-1 elliptical trailing edge thickness ratio instead of the 5-to-1 ratio used by Refs. 13 and 20.

Once both validation cases were completed, nine additional flat-plate wings were tested as shown in Table 2. The flat-plate models were manufactured to the same airfoil configuration as that of the $\mathcal{AR}$ 3 validation wing. A flat-plate airfoil was chosen for testing as it serves as a good baseline to observe and decipher the effects of Reynolds number, aspect ratio, and taper ratio on low-to-moderate aspect ratio wings. In addition, the geometries and Reynolds numbers tested were those typically used for small-scaled UAV wings and stabilizers.

IV. Data Validation

Data validation serves as a method of reinforcing and rechecking the viability of experimental results acquired using a specific wind tunnel balance. Since the LRN-FB was newly designed, the viability of the mounting setup was initially tested. Data validation was then performed on two main test cases for lift, drag and moment.

A. Wing Mounting Setup Viability

The cantilever beam mounting setup for all wings tested made it necessary to account for the tare and interference effects of the sting. As discussed in Ref. 31, the tare of the sting is its direct drag effects, and the interference is its effect on the free air flow over the wing.

The direct drag effects of the sting are accounted for by taking sting tares at the different Reynolds

numbers tested. During wing testing runs, sting tares corresponding to the Reynolds number tested are automatically subtracted prior to calculating the aerodynamic loads.

Two methods were employed to test the interference effects of the sting. For the first test, a mirror sting was mounted to the tunnel floor as shown in Fig. 4(a). Interference tests were done using a Wortmann FX 63-137 $\mathcal{AR}$ 4 rectangular wing. The mirror sting was not attached to the wing. A gap of ≈1 mm was maintained as shown in Fig. 4(b). Tests performed at Reynolds numbers of 30,000 and 60,000 showed that the mirror sting had negligible interference effects on the lift, drag and moment measurements of the wing. In addition, flourescent oil-flow visualization was employed to determine whether the flow over the mounted wings were was substantially affected by the sting. Figure 4(c) shows a photograph of a flourescent oil flow over the upper surface of the Wortmann FX 63-137 $\mathcal{AR}$ 4 wing at $\alpha = 9$ deg and $Re = 90{,}000$. Several important features of low Reynolds number flow over wings were discernible such as the laminar, turbulent, and laminar separation bubble regions. Wing vortex induced separation was also seen at the wing tips. Most importantly, Fig. 4(c) shows that the wing sting caused minimal interference to the flow over the wing.

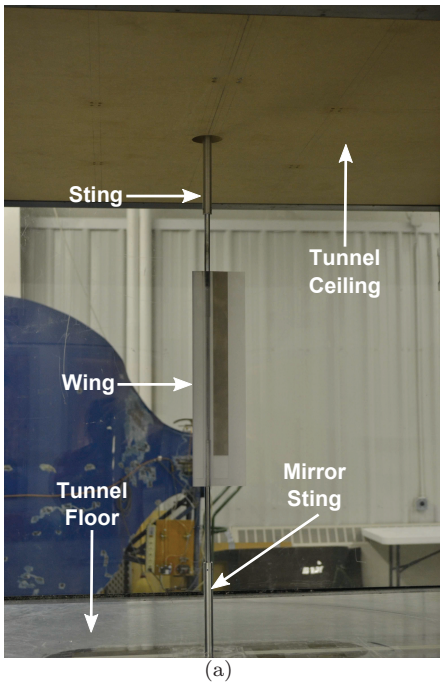

(a)

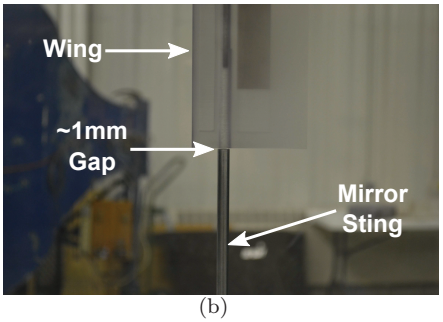

(b)

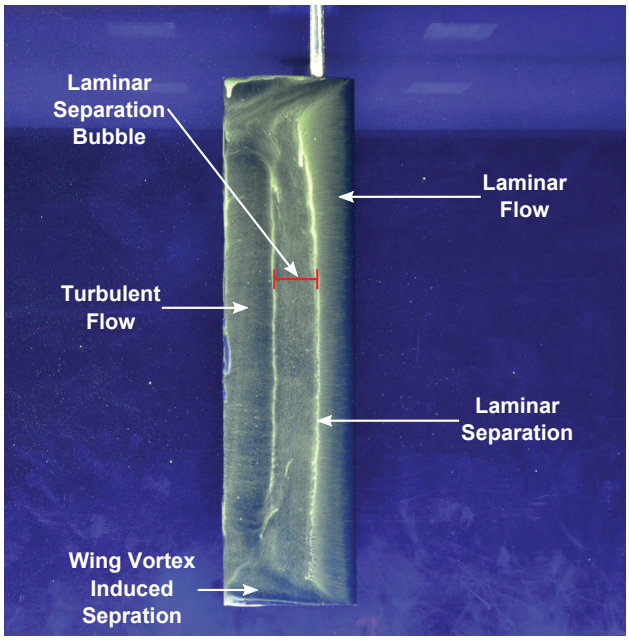

(c)

Figure 4. Sting mirror image setup: (a) Wortmann FX 63-137 $\mathcal{AR}$ 4 wing shown with sting and mirror image, (b) mirror sting to wing gap and, (c) upper surface oil flow visualization of major flow features on the Wortmann FX 63-137 $\mathcal{AR}$ 4 wing ($\alpha = 9$ deg, $Re = 90{,}000$).

B. Wortmann FX 63-137 Wing (Check Standard) Validation

The first and primary data validation case was the Wortmann FX 63-137 $\mathcal{AR}$ 4 wing. The Wortmann wing is also the check standard for future testing with the LRN-FB. Lift and drag validation for the Wortmann wing was performed against historical FX 63-137 $\mathcal{AR}$ 4 wing data from Ref. 23 and Ref. 38. Moment data was compared against two-dimensional airfoil data from Ref. 30. Aerodynamic performance results obtained for the test validation case using the LRN-FB are shown in Figs. 5–7.

Lift data at Reynolds numbers of 80,000 and 100,000 from Bastedo and Mueller[23] and Marchman[38] are co-plotted together with the two-dimensional lift curve slope (2π) and the theoretical lifting line slope for an $\mathcal{AR}$ 4 wing in Figs. 5(a–b). The theoretical lifting line slope for a finite wing of elliptical wing loading is

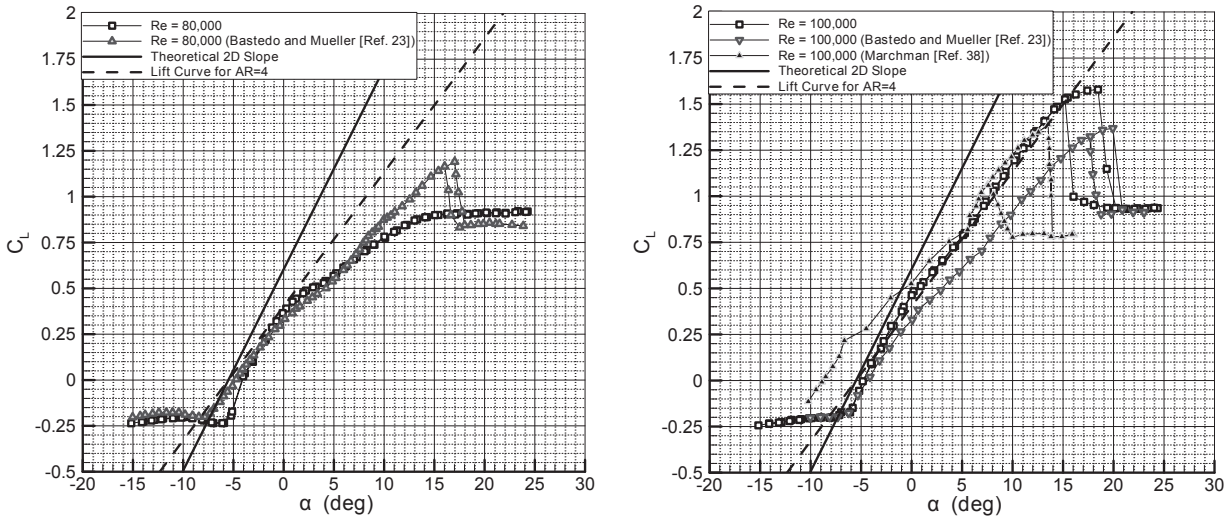

(a) (b)

Figure 5. Lift curve validation for the Wortmann FX 63-137 $\mathcal{AR}$ 4 wing: (a) Re = 80,000 and, (b) Re = 100,000.

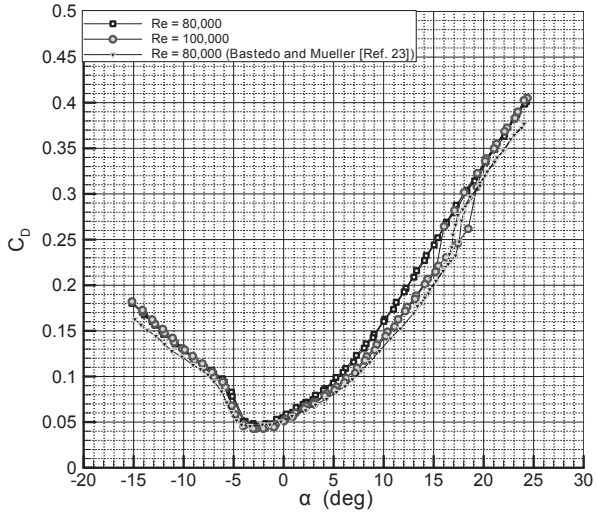

Figure 6. Drag validation for the Wortmann FX 63-137 $\mathcal{AR}$ 4 wing at a Reynolds number of 80,000.

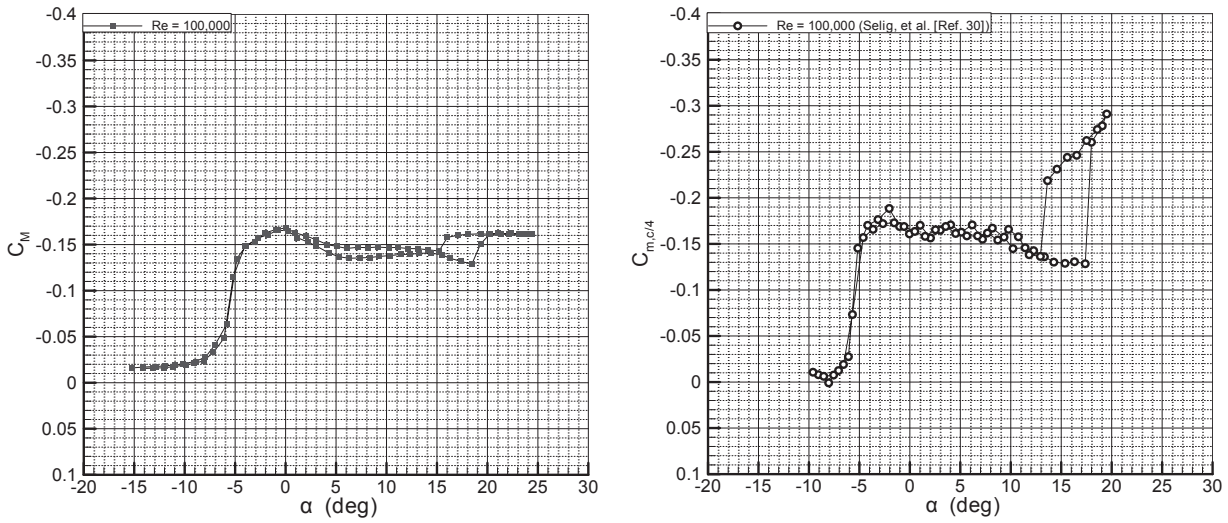

(a) (b)

Figure 7. Moment validation for the Wortmann FX 63-137 $\mathcal{AR}$ 4 wing: (a) Re = 100,000 and, (b) two-dimensional data comparison.

calculated using

$$C_{L\alpha} = C_{l\alpha}\frac{\mathcal{AR}}{\mathcal{AR}+2} \tag{1}$$

Figure 5 shows that the data obtained using the LRN-FB accurately aligns with the theoretical value for an aspect ratio of 4. The data also lies between the historical data.[23,38] The large lift curve slope difference seen in the data from Bastedo and Mueller[23] in Fig. 5(b) may be attributed to their use of semi-span wings. An additional interesting observation from Fig. 5(a) is the higher C_{Lmax} in the historical data, showing that the data from Ref. 23 has a lower critical Reynolds number. As alluded to by Marchman[38] and Shields and Mohseni,[19] the lower critical Reynolds number is likely the result of wind tunnel turbulence quality characteristics. Wind tunnels with higher turbulence levels cause transition to occur at lower Reynolds number due to the increased disturbances in the flow.

Drag comparison plots with Bastedo and Mueller[23] at a Reynolds number of 80,000 and 100,000 are shown in Fig. 6. The general trends and C_{D0} values from the plots show good correlation with the data from Ref. 23. Finally, pitching moment plot comparisons between the LRN-FB data and 2D data from Selig, et al.[30] are plotted in Fig. 7. Both Ref. 23 and 38 did not have pitching-moment data, so only two dimensional data was available. The moment curves from the LRN-FB data in Fig. 7(a) show good correlation with Fig. 7(b) in the characteristics observed. The only large difference is in the post-stall moment characteristics. For a two-dimensional airfoil test, mainly uniform spanwise separation occurs; whereas, for a three-dimensional wing, wing tip vortices prevent flow close to the wing tips from separating. The unseparated flow from the wing tips results in a smaller magnitude difference in post-stall pitching-moment values.

Finally, as an added validation, the key commonality in the data from LRN-FB and historical data at a Reynolds number of 100,000 is the capture of post-stall hysteresis in lift, drag and moment. Post-stall hysteresis will be further discussed in Section V.

C. Flat-Plate $\mathcal{AR}$ 3 Rectangular Wing Validation

An additional validation case was performed on an $\mathcal{AR}$ 3 rectangular ($\lambda = 1$) flat-plate wing. Validation was performed against historical data by Pelletier and Mueller[13] and Shields and Mohseni.[20] The differences between the $\mathcal{AR}$ 3 wing tested with the LRN-FB and that tested by Refs. 13 and 20 were discussed in detail in Section III. Lift, drag, moment and drag polar comparison plots are shown in Figs. 8(a–d).

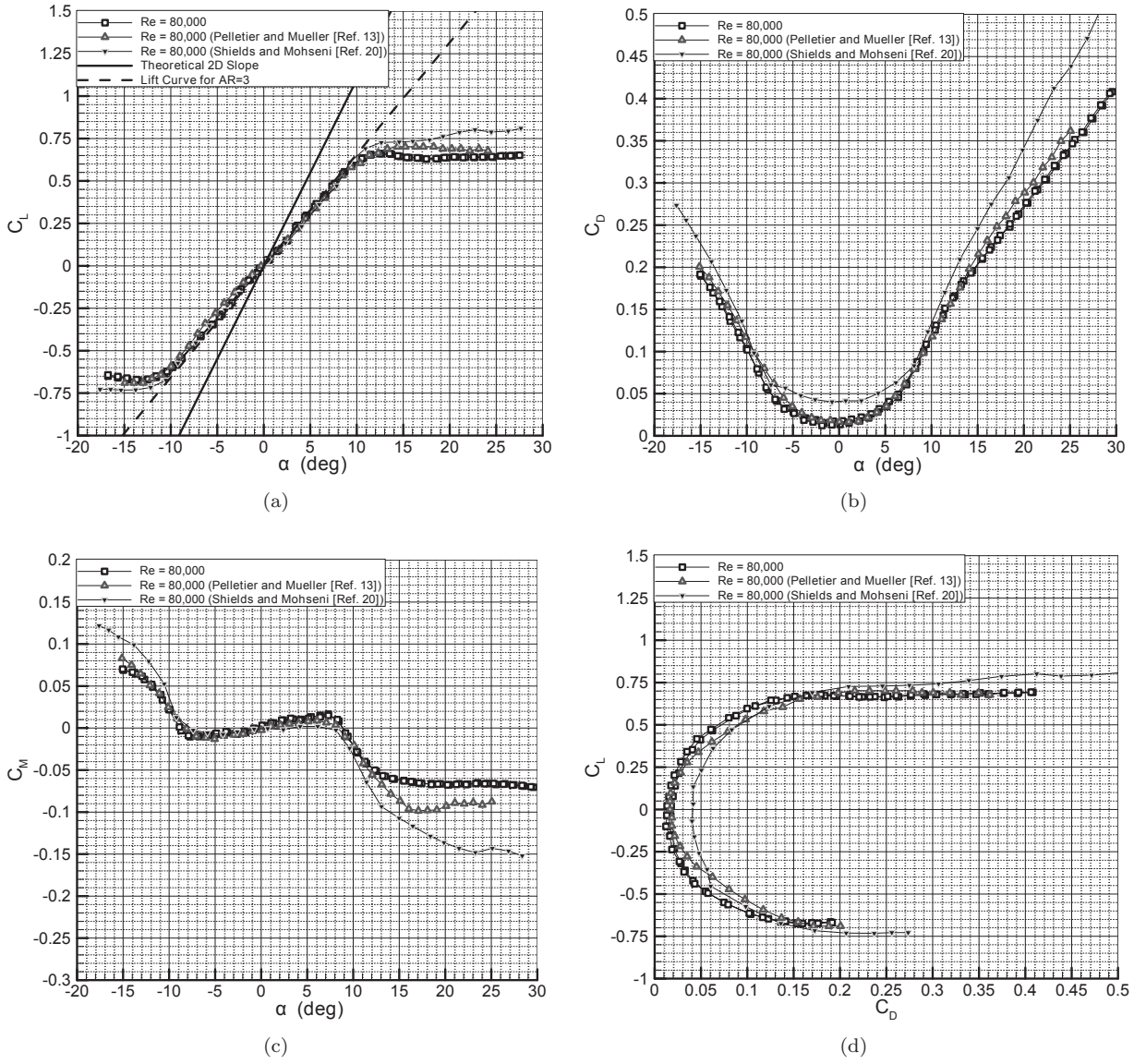

Figure 8. Rectangular $\mathcal{AR}$ 3 flat-plate wing comparison: (a) lift, (b) drag, (c) moment and, (d) drag polar.

Lift comparison plots show close agreement to the theoretical two-dimensional lifting line slope and data from Ref. 13. The only difference is the stall angle of attack and maximum lift coefficient which can be explained by the differences in the models tested as discussed prior. Similarly drag data shows good agreement with Ref. 13. Minor variations are seen in the moment data from Ref. 13 and 20, and it can be attributed as Ref. 20 suggests to experimental setup variations between the three tunnels and test model differences.

V. Experimental Results and Discussion

The LRN-FB was used to measure the performance of the Wortmann FX 63-137 wing over a range of Reynolds numbers. In addition, as mentioned in Section III, ten elliptical leading and trailing edge flat-plate models of varying aspect ratios and taper ratios were tested, and the results are presented.

A. Wortmann FX 63-137 Wing Results

The Wortmann FX 63-137 airfoil has been used extensively in small aircraft and RC models primarily because of its high-lift capabilities at low Reynolds numbers. As a result, the FX 63-137 airfoil and wing have been widely tested in many wind tunnel facilities. It therefore will be beneficial to have a better understanding of the characteristics and differences of a Wortmann $\mathcal{R}$ 4 wing in comparison with the airfoil at low Reynolds numbers. Drag polars, and lift and moment plots at varying Reynolds numbers for the Wortmann FX 63-137 wing are shown in Fig. 9. Data were taken from an angle of attack of −15 to 25 deg at increasing and decreasing angles of attack to capture possible hysteresis effects known to exist in the low Reynolds number regime.

Figure 9 shows that the critical Reynolds number for the Wortmann FX 63-137 wing is 90,000. A jump in lift-to-drag ratio occurs at this Reynolds number. For Reynolds numbers less than 90,000, laminar separation (trailing-edge separation) stall is observed. Laminar separation occurs when the laminar boundary layer over the upper surface of the central section of the wing encounters an adverse pressure gradient that causes it to separate from the wing surface. At Reynolds numbers less than 90,000, the separated laminar boundary or shear layer has insufficient energy to form a laminar separation bubble by transitioning to turbulent flow and reattaching to the wing.

At the critical Reynolds number of 90,000, both pre-stall and post-stall hysteresis phenomena are observed on the FX 63-137 wing. Pre-stall hysteresis, as discussed in Ref. 39, is a type of lift hysteresis that is caused initially by laminar stall with increasing angle of attack. As the angle of attack increases further, the separated laminar shear layer suddenly forms a short laminar separation bubble over the wing. The laminar

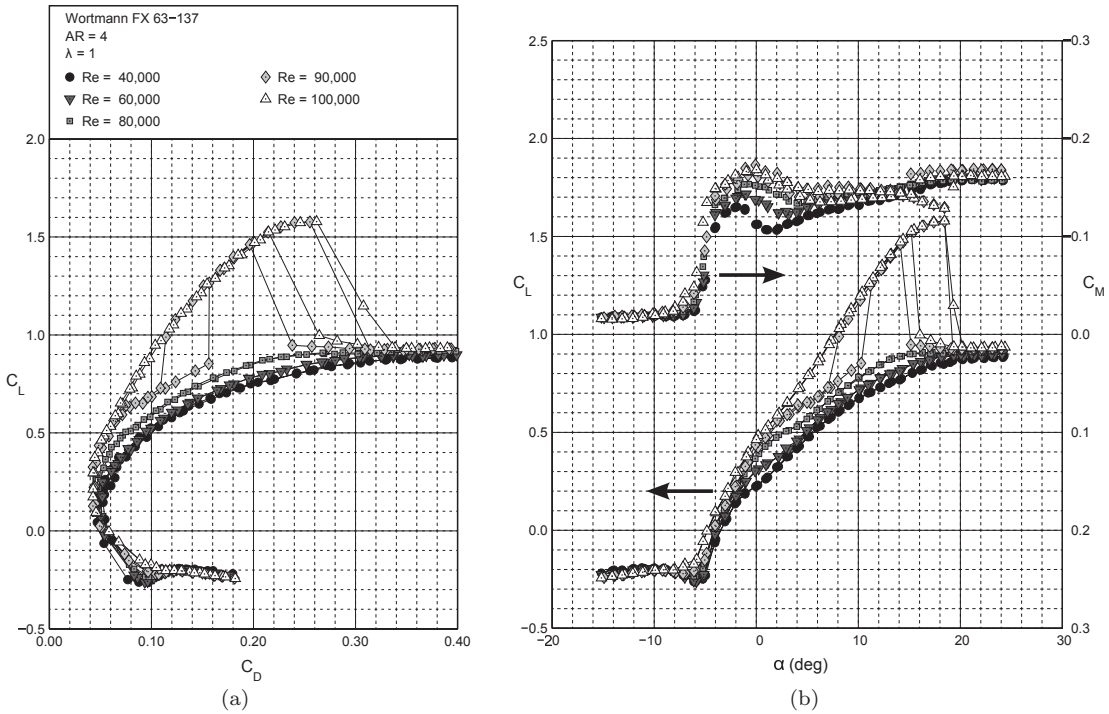

Figure 9. Wortmann FX 63-137 wing with an $\mathcal{R}$ of 4 and λ of 1: (a) drag polars and, (b) lift and moment curves.

separation bubble formation yields a large jump in the lift of the wing and corresponding improvement in the lift-to-drag ratio. The effect of bubble formation is also captured in the drag and moment data. With decreasing angles of attack though, the drop in lift occurs at a lower angle of attack compared with the prior jump. To date, as far as the authors are aware, pre-stall hysteresis has not been captured in literature for FX 63-137 airfoils or wings and has been rarely observed on other airfoils.[40] Although repeatably reproduced, pre-stall hysteresis for the Wortmann wing only occurred at the critical Reynolds number of the Wortmann wing. Any slight changes in the flow speeds resulted in no pre-stall hysteresis.

Post-stall hysteresis is observed and repeatably reproduced at Reynolds numbers of 90,000 and 100,000. Post-stall hysteresis occurs when the laminar separation bubble on the wing upper surface bursts, and flow separation occurs, resulting in a large loss of lift. As angle of attack decreases, however, the laminar separation bubble reattaches at an angle of attack lower than that for which the the burst occurred, creating hysteresis.

Another conclusion that was obtained from the performance plots was that the stall angle of attack is observed to increase with an increase in Reynolds number. Also, it is important to note the increase in the zero-lift angle of attack with decreasing Reynolds number. This trend is similar to that discussed in Bastedo and Mueller.[23]

Surface oil-flow visualization tests were performed at a number of angles of attack to further understand the interesting flow phenomena on the Wortmann wing at a Reynolds number of 90,000. Figures 10(a–h) shows photographs of the upper surface of the Wortmann wing at these different angles of attack. Laminar flow accompanied by a flow separation or a long separation bubble is seen at -2 and 7 deg. The location of the bubble moves toward the leading edge of the wing with increasing angle of attack. For both these angles of attack, it can be also observed that turbulent flow has not fully developed over the trailing-edge section of the wing. At 9 deg, the long bubble 'collapses' into a short separation bubble. Fully developed turbulent flow is also seen at the trailing edge of the wing. It can be concluded that because the short separation bubble formed, the jump in the lift for the wing has prematurely occurred and that the pre-stall hysteresis stage was bypassed. The premature tripping of the wing boundary layer may have been caused by the slight roughness of the wing surface by the flow visualization oil.

The short separation bubble is seen to further move toward the leading edge and shrink at 12 deg. A small laminar flow region is seen at an angle of attack of 14 deg with the separation bubble and turbulent regions convering most of the upper surface of the wing. From -2 to 14 deg, a steady growth is observed in the disturbance caused by the wing tip vortices. The steady growth is caused by the strength of wing tip vortices that increase with lift. At 18 deg, the bubble is not present, and the steady bands of oil on the upper surface of the wing represent the fully tubulent region of the flow over the wing. Finally, at 22 deg, the unaltered oil flow indicates complete flow separation from the upper surface of the wing. Post-stall hysteresis was captured when the angle of attack of the wing was initially set to 22 deg and then reduced to 18 deg during a flow visualization test run. Figure 10(h) shows that the flow was still fully separated in comparison with the fully turbulent flow in Fig. 10(f).

B. Flat-Plate Rectangular Wing Results

For the flat plate tests, drag polars, and lift and moment plots are shown for all ten flat plate wings described in Section III. Data was taken from -20 to 30 deg for increasing and decreasing angles of attack. A large angle of attack range was chosen to capture post-stall effects of the flat-plate wing.

The drag polars, and lift and moment plot from Figs. 11–20 shows a number of interesting observations related to an increase in Reynolds number. Firstly, there is a widening of the drag bucket with increasing Reynolds number. The widening of the drag bucket suggests a reduction in the degree of separated flow over the flat-plate wing when the flow speed increases. Theoretically, C_{Dmin} should decrease with Reynolds number. The decreasing C_{Dmin} is generally seen for wings of $\mathcal{R}$ 3 to 5. Aspect ratio 2 wings, however, show scatter in the C_{Dmin} values. The scatter can be attributed to the low forces that were measured that were within the uncertainty levels of the LRN-FB.

For the lift curves, an obvious increase in lift curve slope and C_{Lmax} is seen. Stall occurs as a result of laminar separation as it is not accompanied by a large drop in lift, and a critical Reynolds number is not observed. The lack of a critical Reynolds number suggests that the laminar boundary (shear) layer that separates from the central region of the flat-plate wing was unable to reattach resulting in no laminar

separation bubbble formation. For post-stall angles of attack, the lift and moment of the wing stays roughly the same; however, there is a corresponding decrease of lift-to-drag ratio of the wing that results from an increase in the wake drag with angle of attack. Finally, no flow hysteresis was observed.

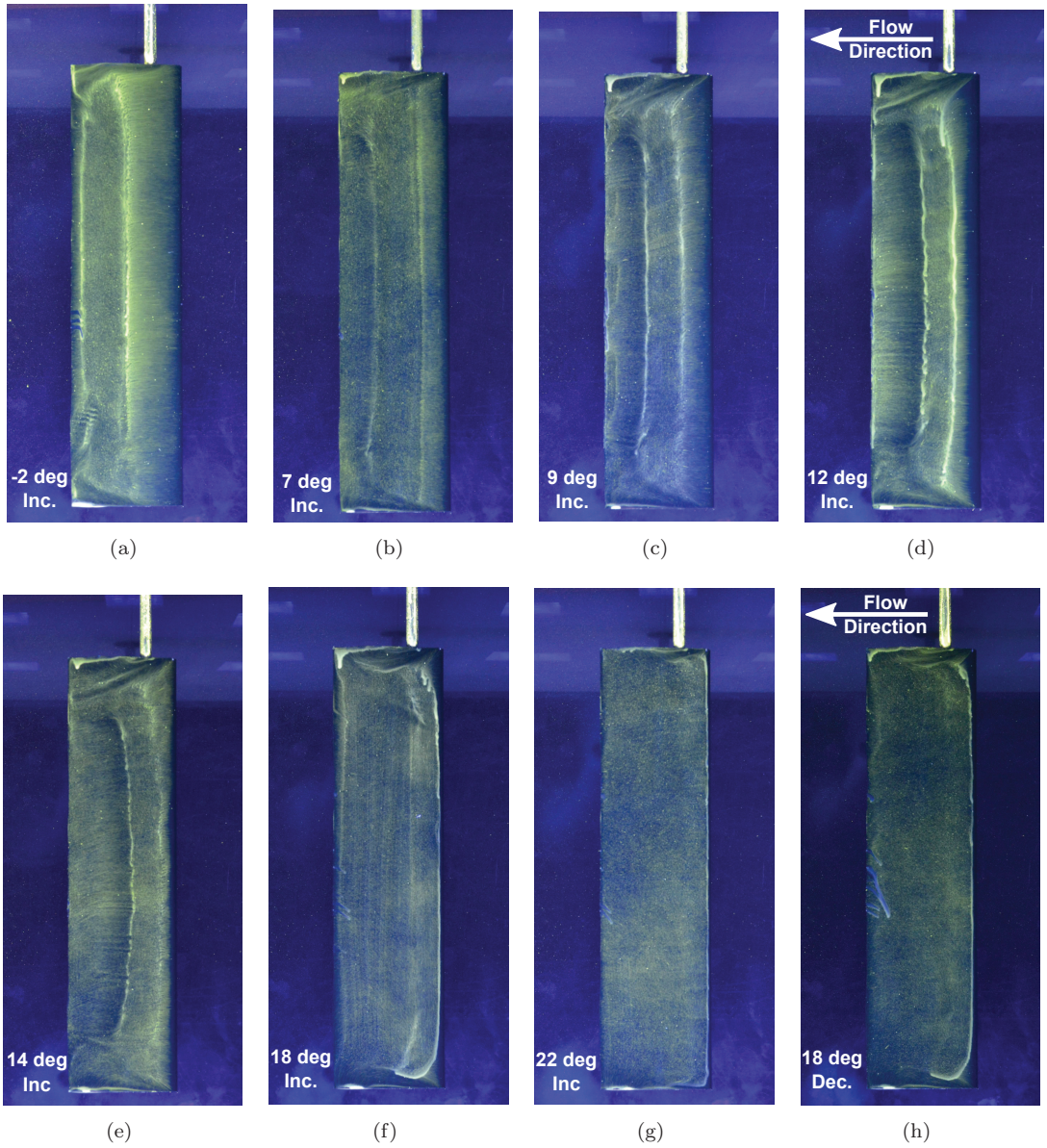

Figure 10. Upper surface oil flow visualization of major flow features on the Wortmann FX 63-137 $\mathcal{AR}$ 4 λ 1 wing at a Re of 90,000: (a) $\alpha = -2$ deg (increasing AOA), (b) $\alpha = 7$ deg (increasing AOA), (c) $\alpha = 9$ deg (increasing AOA), (d) $\alpha = 12$ deg (increasing AOA), (e) $\alpha = 14$ deg (increasing AOA), (f) $\alpha = 18$ deg (increasing AOA), (g) $\alpha = 22$ deg (increasing AOA) and, (h) $\alpha = 18$ deg (decreasing AOA).

VI. Conclusions

In conclusion, an area of experimental research needed in the low Reynolds number regime was examined. A new force/moment balance, the LRN-FB was designed, fabricated and assembled to carry out these new measurements. The LRN-FB was validated for low Reynolds number, low-to-moderate aspect ratio wings by flow visualization techniques and data comparisons with historical data. Historical data comparisons showed good agreement in lift, drag and moment data. Experimental tests and surface oil-flow visualization tests showed that the sting had minimal interference effects on the flow over a wing.

As a check standard test and to further understand flow phenomena over low-to-moderate aspect ratio wings, aerodynamic performance results and flow visualizations results were presented for the Wortmann FX 63-137 $\mathcal{AR}$ 4 rectangular wing. The results suggested that there exists a critical Reynolds number ($Re = 90{,}000$) for which a jump in lift and lift-to-drag ratio occurs. In addition, both pre-stall and post-stall hysteresis were captured at this Reynolds number. Finally, flow visualization was used to chart and discuss the progress of the laminar, separation bubble, turbulent and wing tip region with change in angle of attack at a Reynolds number of 90,000. With flow visualization, pre-stall hysteresis was not captured, but post-stall hysteresis was captured successfully.

Results were also presented for ten rectangular and tapered, flat-plate, low aspect ratio wings at Reynolds numbers of 60,000 to 160,000. The results obtained suggested that for flat plates, there is either no critical Reynolds number or that the critical Reynolds number does not seem to lie between the Reynolds numbers of 60,000 and 160,000. Aerodynamic hysteresis was found to not exist for the flat-plate wings at the present test conditions. Finally, the post-stall data for the flat-plate wings show that lift and moment are relatively constant with increasing angles of attack up to 30 deg.

References

[1]Kellogg, J. C., "Case Study: Micro Tactical Expendable Rigid-Wing Micro Air Vehicle," *Introduction to the Design of Fixed-Wing Micro Air Vehicles*, edited by T. J. Mueller, J. C. Kellogg, P. G. Ifju, and S. V. Shkarayev, AIAA Educational Series, AIAA, Reston, VA, pp. 151—184.

[2]Ailinger, K., "Micro Air Vehicle (MAV) Development at NRL," Association of Unmanned Vehicle Systems International Conference 1997 (AUVSI '97), Arlington, VA, June 1997.

[3]Kellogg, J., Bovais, C., Foch, J., Gardner, R., Gordon, D., Hartley, R., Kamgar-Parsi, B., McFarlene, H., Pipitone, F., Ramamurthy, R., Sciambi, R., Spears, W., Scrull, D., and Sullivan, C., "The NRL Micro Tactical Expendable (MITE) Air Vehicle," *The Aeronautical Journal*, 106(1062), August 2002, pp. 431–441.

[4]Grassmeyer, J. M. and Keennon, M. T., "Development of the Black Widow Micro Air Vehicle," AIAA Paper 2001–0127, Reno, NV, Jan. 2001.

[5]Ifju, P., Jenkins, D., Ettinger, S., Lian, Y., Shyy, W., and Waszak, M., "Flexible-wing-based micro air vehicles," AIAA Paper 2002–0705, Reno, NV, Jan. 2002.

[6]Lian, Y. and Shyy, W., "Three Dimensional Fluid Structure Interactions of a Membrane Wing for MAV Applications," AIAA Paper 2003–1726, Norfolk, VA, April 2003.

[7]Albertani, R., *Experimental Aerodynamic of Elastic Deformation Characterization of Low Aspect Ratio Finite Wings Applied to Micro Air Vehicles*, Ph.D. thesis, Dept. of Mechanical and Aerospace Engineering, University of Florida, Gainesville, FL, 2005.

[8]Albertani, R., Stanford, B., Hubner, J., and Ifju, P., "Aerodynamic Characterization and Deformation Measurements of a Flexible Wing Micro Air Vehicle," *Experimental Mechanics*, Vol. 47, No. 5, 2007, pp. 625–635.

[9]Null, W. and Shkarayev, S., "Effects of Camber on the Aerodynamics of Adaptive-Wing Micro Air Vehicles," *Journal of Aircraft*, Vol. 42, No. 6, Nov.–Dec. 2005, pp. 1537–1542.

[10]Null, W., Noseck, A., and Shkarayev, S., "Effects of Propulsive-Induced Flow on the Aerodynamics of Micro Air Vehicles," AIAA Paper 2005–4616, Toronto, Ontario, June 2005.

[11]Shkarayev, S., Moschetta, J.-M., and Bataille, B., "Aerodynamic Design of Micro Air Vehicles for Vertical Flight," *Journal of Aircraft*, Vol. 45, No. 5, Sept.–Oct. 2008, pp. 1715–1724.

[12]Torres, G. E. and Mueller, T. J., "Low-Aspect-Ratio Wing Aerodynamics at Low Reynolds Numbers," *Journal of Aircraft*, Vol. 42, No. 5, May 2004, pp. 865–873.

[13]Pelletier, A. and Mueller, T. J., "Low Reynolds Number Aerodynamics of Low-Aspect-Ratio Thin/Flat/Cambered-Plate Wings," *Journal of Aircraft*, Vol. 37, No. 5, Sept.–Oct. 2000, pp. 825–832.

[14]Mueller, T. J. and DeLaurier, J. D., "Aerodynamics of Small Vehicles," *Annual Review of Fluid Mechanics*, Vol. 35, Jan. 2003, pp. 89–111.

[15]Mueller, T. J., "Aerodynamic Measurements at Low Reynolds Numbers for Fixed Wing Micro-Air Vehicles," RTO AVT/VKI Special Course, Rhode-St-Genèse, Belgium, Sept. 1999.

[16]Kaplan, S. M., Altman, A., and Ol, M., "Wake Vorticity Measurements for Low Aspect Ratio Wings at Low Reynolds Numbers," *Journal of Aircraft*, Vol. 44, No. 1, 2007, pp. 241–251.

[17]Moschetta, J.-M. and Thipyopas, C., "Aerodynamic Performance of a Biplane Micro Air Vehicle," *Journal of Aircraft*, Vol. 44, No. 1, 2007, pp. 291–299.

[18]Lupo, S., Nyberg, H., Karlsson, A., and Mohnseni, K., "Xwing – A 3D Viscous Design Tool for Wings," AIAA Paper 2008–0173, Reno, NV, Jan. 2008.

[19]Shields, M. and Mohnseni, K., "Experimental Complications Inherent to Low Reynolds Number Wind Tunnel Testing," AIAA Paper 2011–0873, Orlando, FL, Jan. 2011.

[20]Shields, M. and Mohseni, K., "Effects of Sideslip on the Aerodynamics of Low-Aspect-Ratio Low-Reynolds-Number Wings," *AIAA Journal*, Vol. 50, No. 1, Jan. 2012, pp. 85–99.

[21]Pines, D. J. and Bohorquez, F., "Challenges Facing Future Micro-Air-Vehicle Development," *Journal of Aircraft*, Vol. 43, No. 2, March–April 2006, pp. 290–305.

[22]Cosyn, P. and Vierendeels, J., "Numerical Investigation of Low-Aspect-Ratio Wings at Low Reynolds Numbers," *Journal of Aircraft*, Vol. 43, No. 3, May–June 2006, pp. 713–722.

[23]Bastedo, W. G., Jr. and Mueller, T. J., "Spanwise Variation of Laminar Separation Bubbles on Wings at Low Reynolds Numbers," *Journal of Aircraft*, Vol. 23, No. 9, Sept. 1986, pp. 687–694.

[24]Laitone, E. V., "Wind Tunnel Tests of Wings at Reynolds Numbers below 70,000," *Experiments in Fluids*, Vol. 23, 1997, pp. 405–409.

[25]Okamoto, M. and Azuma, A., "Aerodynamic Charateristics at Low Reynolds Number for Wings of Various Plansforms," *Journal of Aircraft*, Vol. 49, No. 6, June 2011, pp. 1135–1150.

[26]Selig, M. S., Donovan, J. F., and Fraser, D. B., *Airfoils at Low Speeds*, Soartech 8, SoarTech Publications, Virginia Beach, VA, 1989.

[27]Selig, M. S., Guglielmo, J. J., Broeren, A. P., and Giguère, P., *Summary of Low-Speed Airfoil Data*, Vol. 1, SoarTech Publications, Virginia Beach, VA, 1995.

[28]Selig, M. S., Lyon, C. A., Giguère, P., Ninham, C. N., and Guglielmo, J. J., *Summary of Low-Speed Airfoil Data*, Vol. 2, SoarTech Publications, Virginia Beach, VA, 1996.

[29]Lyon, C. A., Broeren, A. P., Giguère, P., Gopalarathnam, A., and Selig, M. S., *Summary of Low-Speed Airfoil Data*, Vol. 3, SoarTech Publications, Virginia Beach, VA, 1997.

[30]Selig, M. S. and McGranhan, B. D., "Wind Tunnel Aerodynamic Tests of Six Airfoils for Use on Small Wind Turbines," National Renewable Energy Laboratory, NREL/SR-500-35515, Golden, CO, 2004.

[31]Barlow, J. B., Rae, W. H., Jr., and Pope, A., *Low-Speed Wind Tunnel Testing*, John Wiley and Sons, New York, 3rd ed., 1999.

[32]Lam, S. S. W., "A FORTRAN program for the Calculation of the Calibration Coefficient of a Six-Component Strain Gauge Balance." Flight Mechanics Technical Memorandum 410, Aeronautical Research Laboratory, Defence Science and Technology Organisation, Melbourne, Australia, 1989.

[33]Leung, S. Y. F. and Link, Y. Y., "Comparison and Analysis of Strain Gauge Balance Calibration Matrix Mathematical Models." DSTO 857, Aeronautical and Maritime Research Laboratory, Defence Science and Technology Organisation, Melbourne, Australia, 1999.

[34]Ramaswamy, M. A., Srinivas, T., and Holla, V. S., "A Simple Method for Wind Tunnel Balance Calibration Including Non-Linear Interaction Terms." Proceedings of the ICIASF '87 RECORD, New York, NY, 1987.

[35]Kline, S. and McClintock, F. A., "Describing Uncertainty in Single-Sample Experiments," *Mechanical Engineering*, Vol. 75, 1953, pp. 3–8.

[36]Coleman, H. W. and Steele, W. G., Jr., *Experimentation and Uncertainty Analysis For Engineers*, John Wiley and Sons, New York, 1989.

[37]Anonymous, "Realize,® Inc. Rapid Prototyping, Rapid Prototypes, Stereolithography," http://www.realizeinc.com/, Accessed Feb. 2012.

[38]Marchman, J. F., "Aerodynamic Testing at Low Reynolds Numbers," *Journal of Aircraft*, Vol. 24, No. 2, Feb. 1987, pp. 107–114.

[39]Selig, M. S., "The Design of Airfoils at Low Reynolds Numbers," AIAA Paper 1985–0074, Reno, NV, Jan. 1985.

[40]Althaus, D., *ProfilePolaren Fur den Modellflug (Windkanalmessungen an Profile im Kritischen Reynoldszahlbereich)*, Necker-Verlag, Villingen-Schwenningen, Germany, 1980.

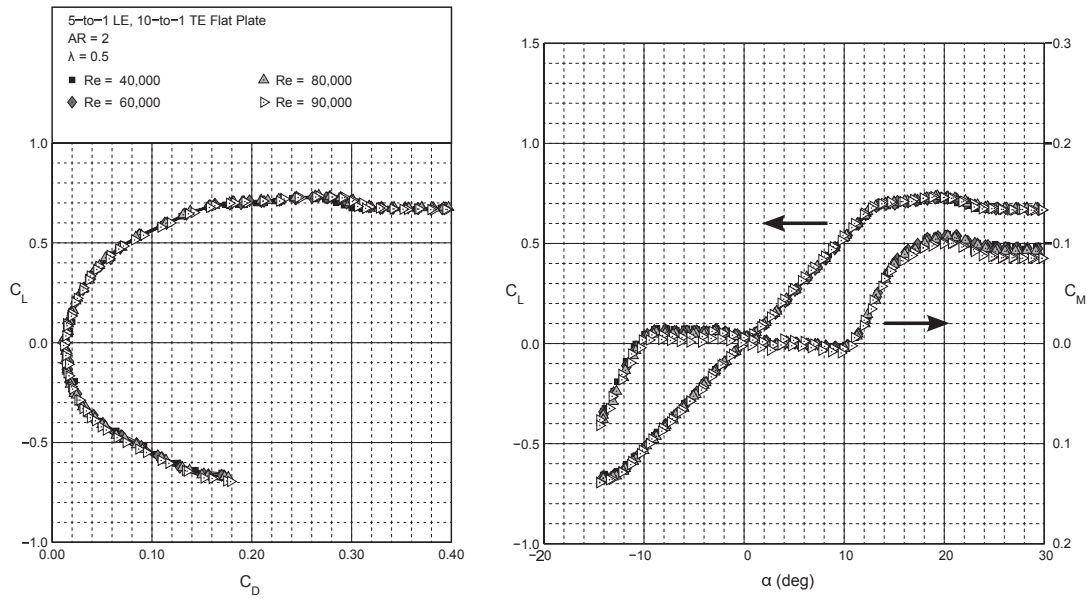

Figure 11. 5-to-1 LE, 10-to-1 TE flat-plate wing with an $\mathcal{AR}$ of 2 and λ of 0.5: (a) drag polars and, (b) lift and moment curves.

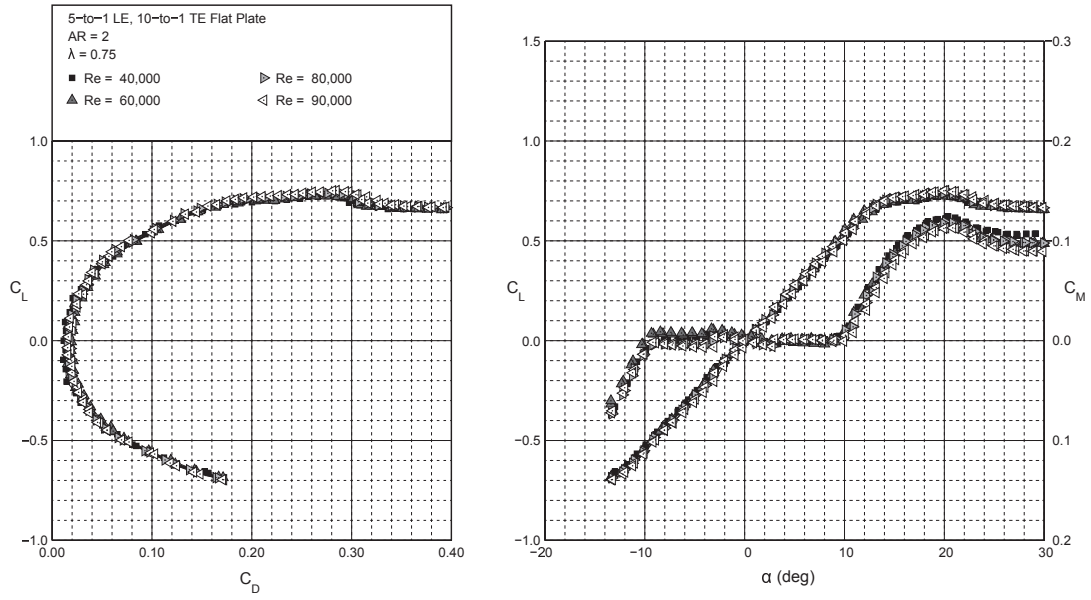

Figure 12. 5-to-1 LE, 10-to-1 TE flat-plate wing with an $\mathcal{AR}$ of 2 and λ of 0.75: (a) drag polars and, (b) lift and moment curves.

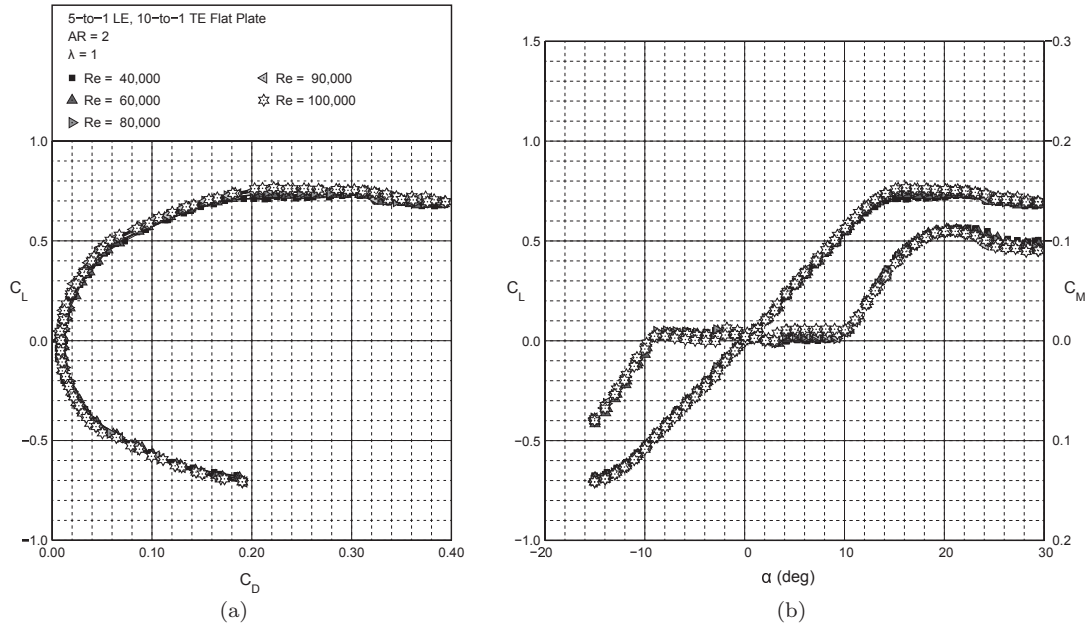

Figure 13. 5-to-1 LE, 10-to-1 TE flat-plate wing with an $\mathcal{AR}$ of 2 and λ of 1: (a) drag polars and, (b) lift and moment curves.

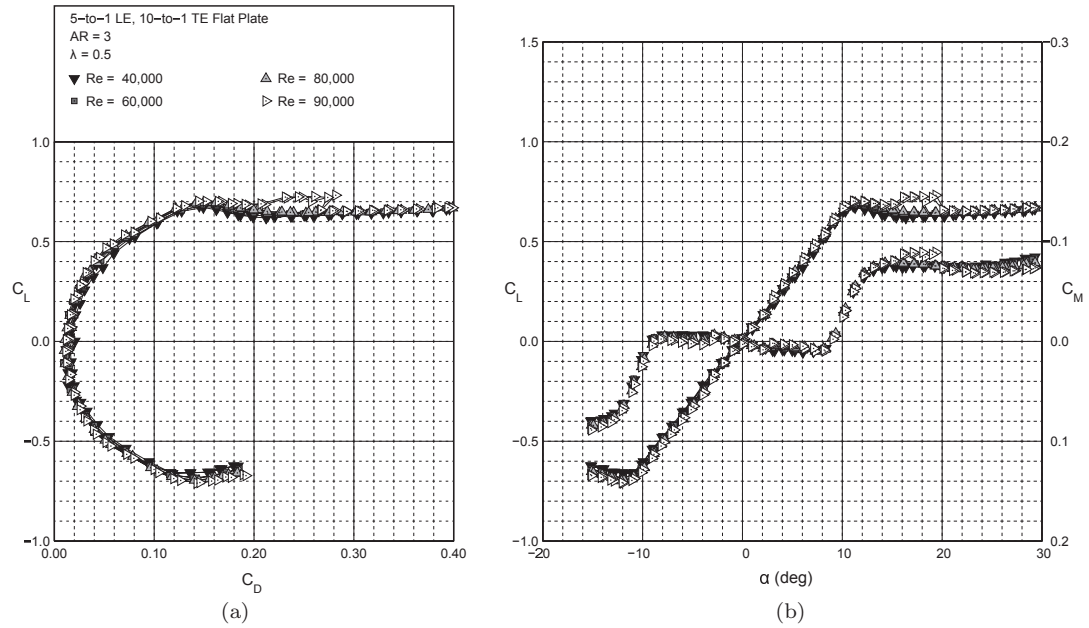

Figure 14. 5-to-1 LE, 10-to-1 TE flat-plate wing with an $\mathcal{AR}$ of 3 and λ of 0.5: (a) drag polars and, (b) lift and moment curves.

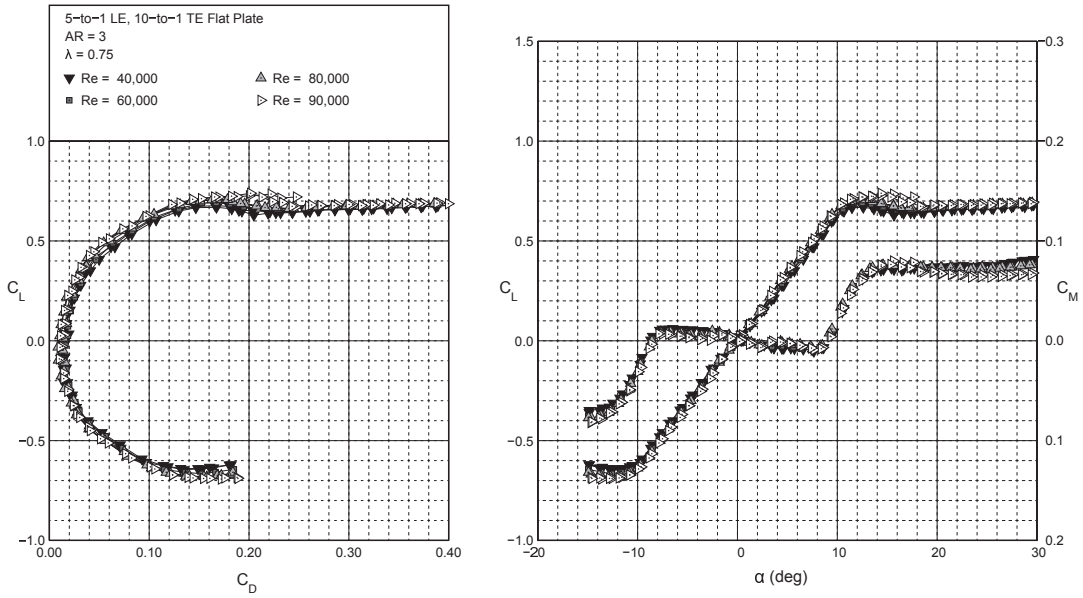

Figure 15. 5-to-1 LE, 10-to-1 TE flat-plate wing with an $\mathcal{AR}$ of 3 and λ of 0.75: (a) drag polars and, (b) lift and moment curves.

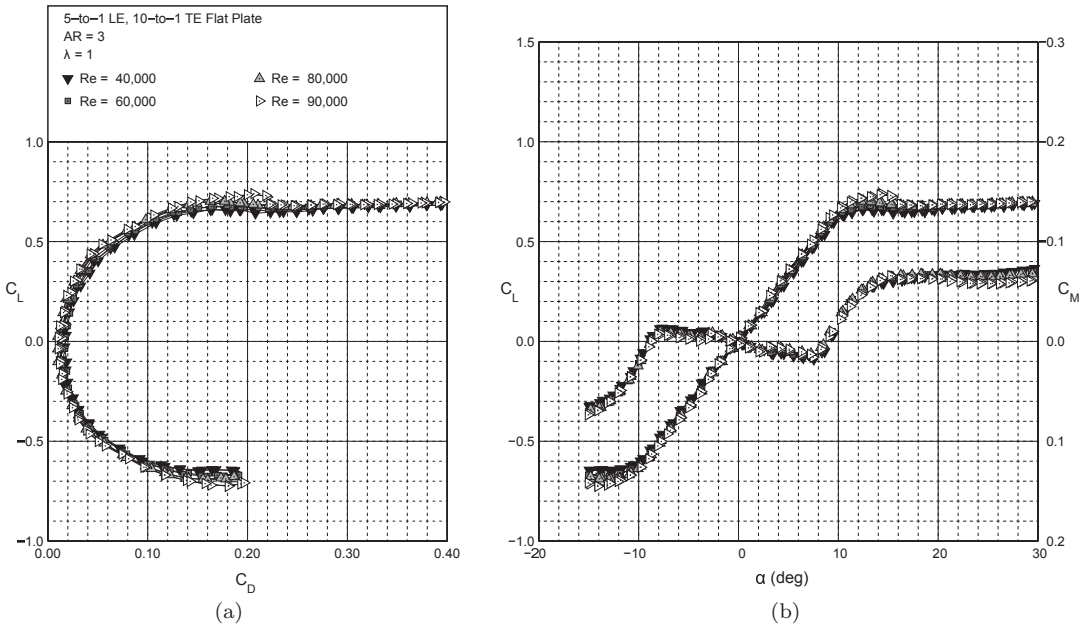

Figure 16. 5-to-1 LE, 10-to-1 TE flat-plate wing with an $\mathcal{AR}$ of 3 and λ of 1: (a) drag polars and, (b) lift and moment curves.

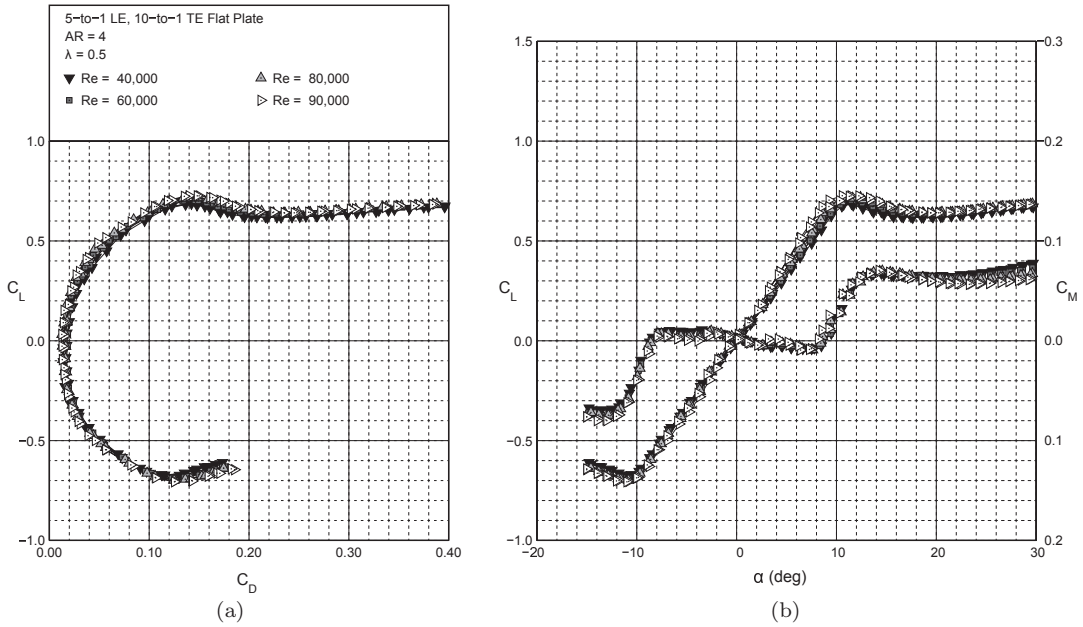

Figure 17. 5-to-1 LE, 10-to-1 TE flat-plate wing with an $\mathcal{AR}$ of 4 and λ of 0.5: (a) drag polars and, (b) lift and moment curves.

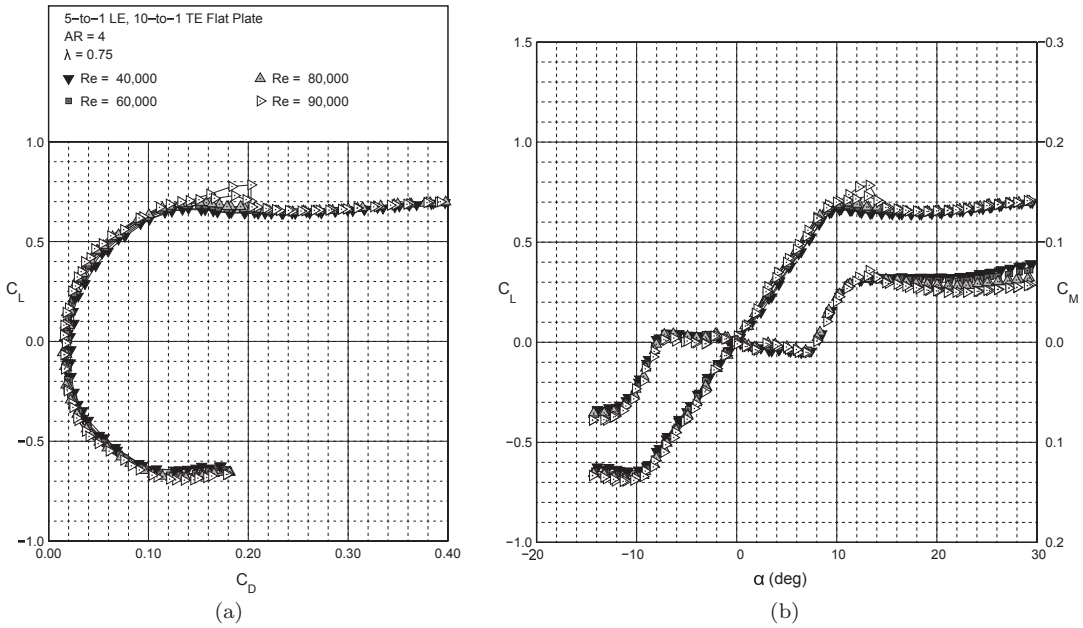

Figure 18. 5-to-1 LE, 10-to-1 TE flat-plate wing with an $\mathcal{AR}$ of 4 and λ of 0.75: (a) drag polars and, (b) lift and moment curves.

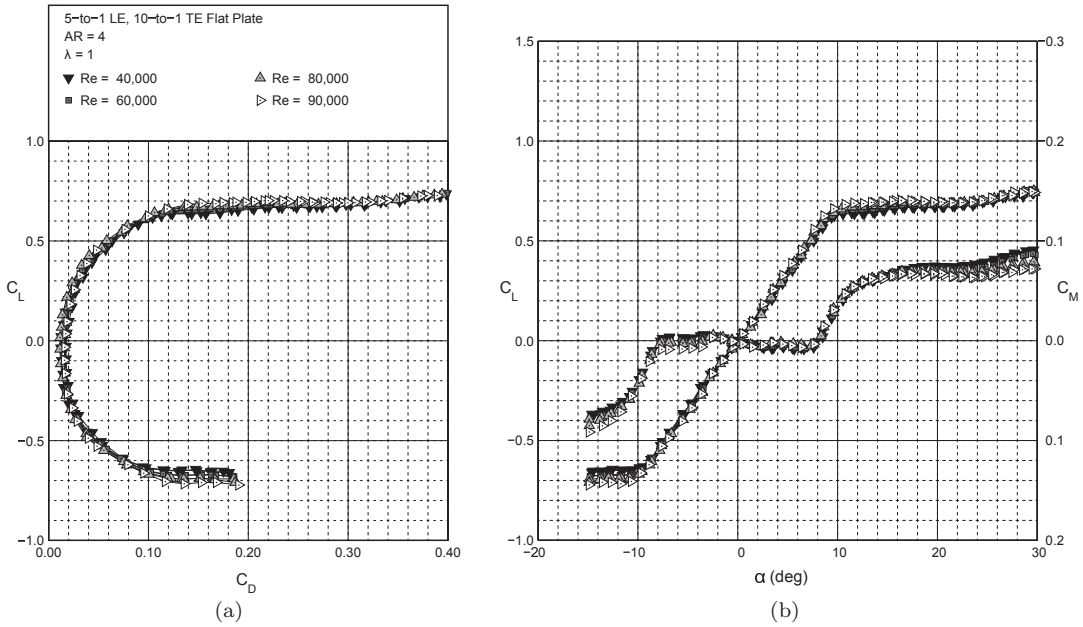

Figure 19. 5-to-1 LE, 10-to-1 TE flat-plate wing with an $\mathcal{AR}$ of 4 and λ of 1: (a) drag polars and, (b) lift and moment curves.

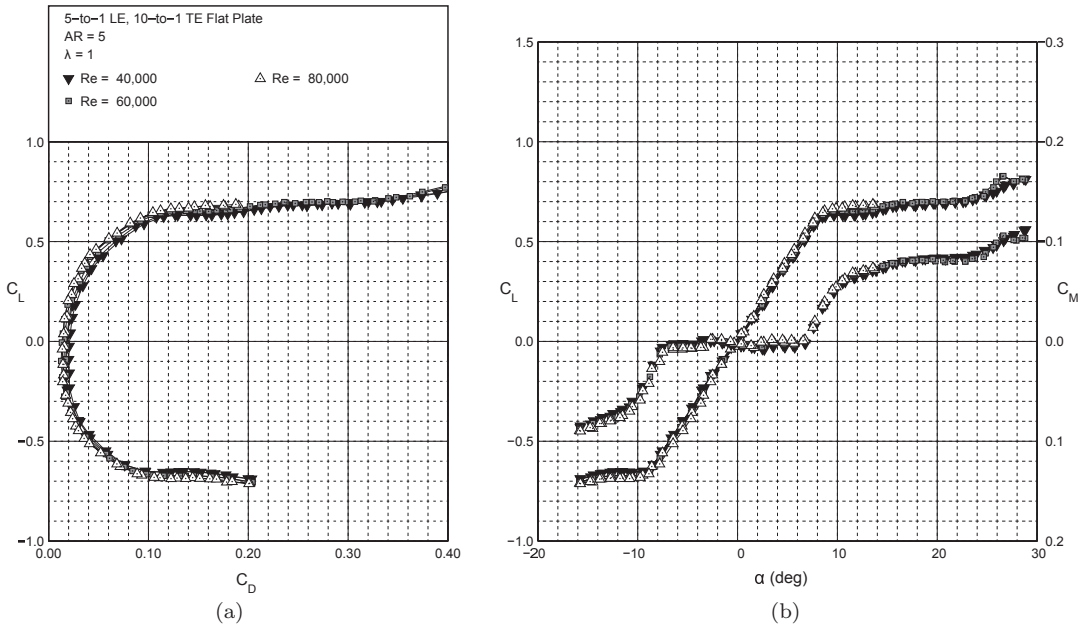

Figure 20. 5-to-1 LE, 10-to-1 TE flat-plate wing with an $\mathcal{AR}$ of 5 and λ of 1: (a) drag polars and, (b) lift and moment curves.